BIOPHYSICS

Strictures of a microchannel impose fierce competition to select for highly motile sperm

Meisam Zaferani[1], Gianpiero D. Palermo[2], Alireza Abbaspourrad[1]*

Investigating sperm locomotion in the presence of external fluid flow and geometries simulating the female reproductive tract can lead to a better understanding of sperm motion during fertilization. Using a microfluidic device featuring a stricture that simulates the fluid mechanical properties of narrow junctions inside the female reproductive tract, we documented the gate-like role played by the stricture in preventing sperm with motilities below a certain threshold from advancing through the stricture to the other side (i.e., fertilization site). All the slower sperm accumulate below (i.e., in front of) the stricture and swim in a butterfly-shaped path between the channel walls, thus maintaining the potential for penetrating the stricture and ultimately advancing toward the fertilization site. Accumulation below the stricture occurs in a hierarchical manner so that dense concentrations of sperm with higher velocities remain closer to the stricture, with more sparsely distributed arrays of lower-velocity sperm lagging behind.

INTRODUCTION

In mammals, the number of sperm entering the female reproductive tract (~60 million to 100 million) exceeds the number of available eggs (one egg during every ovulation) by far (*1*). Accordingly, only a few sperm can fertilize the available eggs. Since motility is required for sperm to traverse the female genital tract (*2*), it has been thought that normal motility is one of the critical properties that determine the sperm's fertilization chances (*3*). Consequently, motility-based competition must take place so that sperm with higher motility have a greater chance of fertilizing the egg (*4*).

In addition to motility, sperm require steering mechanisms to swim on the correct path toward the egg (*5*). Chemotaxis (*6*) has been identified as a steering mechanism for the sperm of marine invertebrates, such as sea urchins (*7*–*13*). However, its role in the guidance of mammalian sperm toward the egg is disputable (*14*). In mammals, the fluid mechanical steering mechanisms of sperm, including the tendency to follow rigid boundaries (*15*, *16*) and swim upstream (i.e., sperm rheotaxis) (*17*–*19*), are known to be responsible for guiding sperm toward the egg. Swimming along rigid boundaries enables sperm to move parallel to the walls of the female reproductive tract, and the rheotactic behavior leads to their ability to swim opposite to the directional flow of secreted genital mucus (*20*–*23*). Since the fluid mechanical steering mechanisms solely guide motile sperm, all nonmotile sperm are carried away by the genital mucus flow, while the healthy, motile sperm advance toward the fertilization site (*23*). This ability of the motile sperm to swim upstream has been used to design new microfluidic tool to hasten the process of sperm separation required for assisted reproductive technologies (*24*).

To date, mammalian sperm locomotion, including its fluid mechanical steering mechanisms, has been studied using microfluidic technology (*16*, *18*). However, the sperm rheotaxis–based navigation in the presence of a fluid flow has been examined exclusively in straight swimming channels (*17*, *20*, *21*, *23*), whereas the biophysical/fluid mechanical conditions of the female reproductive tract are more complex (*25*, *26*). The sperm swimming channel within the female reproductive tract does not have constant dimensions, but rather varies in width. Deviation in width of the swimming channel results in alteration of the flow magnitude, which consequently influences the sperm rheotactic and boundary swimming behavior. Therefore, investigation of sperm locomotion in a channel that mimics the biophysical aspects of the swimming channel in vivo will reveal the impact of the channel geometry on the sperm-steering mechanisms. By the same token, the effect of the fluid mechanical properties of the female reproductive tract on motility-based competition among sperm cells can be revealed.

In this study, we examine sperm motion, including their fluid mechanical steering mechanisms, by solving sperm equations of motion inside a microfluidic design featuring variable width. In addition, by experimentally observing sperm locomotion within the design, we show that strictures inside the sperm swimming channel play a gate-like role. That is, sperm slower than a threshold velocity cannot pass through the stricture, revealing the function of narrow junctions in the reproductive tract in selecting for highly motile sperm. Sperm slower than the threshold velocity resist against the flow and accumulate below (i.e., in front of) the stricture in a hierarchical manner in which motility-based competition becomes fiercer among highly motile sperm.

RESULTS AND DISCUSSION

We designed and fabricated a microfluidic device with 30 μm in depth using conventional soft lithography that featured three eye-shaped compartments connected to each other by a progressive narrowing in width of the microchannel (Fig. 1A). The width of the channel in the narrowest section (i.e., the stricture) was 40 μm, while the maximum width of each compartment was 300 μm. The angle of the stricture mouth was ~ 80 °. The velocity field of the sperm medium (i.e., shear rate along the $\hat{z}$ and $\hat{y}$ directions) within each stricture was designed to be high enough to act as a barrier so that no sperm can pass through. The velocity field within the microfluidic channel was obtained by solving the conservation of momentum and mass equations with no-slip boundary conditions using finite element method simulations. The velocity field in an X-Y cut plane at a Z position corresponding to half the channel depth is demonstrated in Fig. 1A, which shows that the mean velocity field increases as the

[1]Department of Food Science and Technology, Cornell University, Ithaca, NY 14853, USA. [2]The Ronald O. Perelman and Claudia Cohen Center for Reproductive Medicine, Weill Cornell Medicine, New York, NY 10021, USA.
*Corresponding author: alireza@cornell.edu

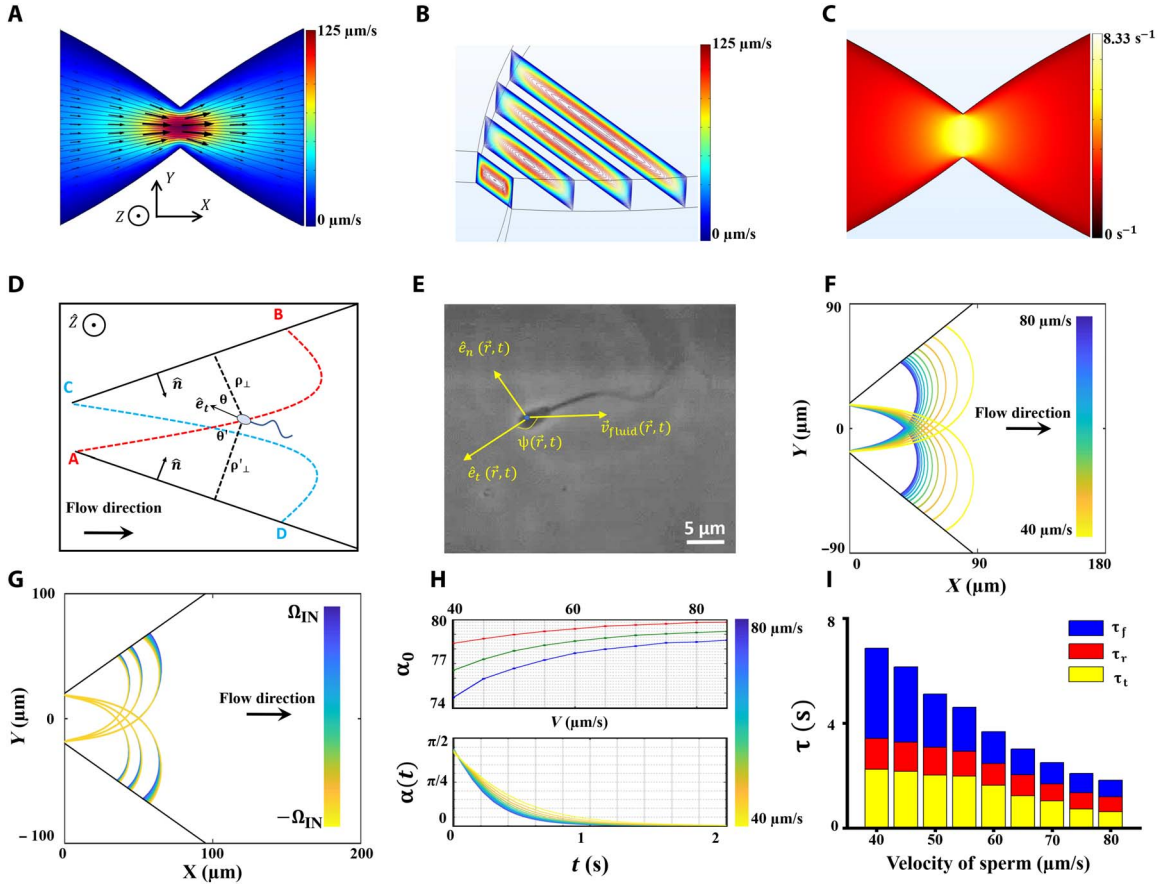

Fig. 1. Simulation of sperm motion below the stricture. (**A**) Two-dimensional velocity field of the sperm medium within the device at $Z = 15$ μm. (**B**) Velocity field of the medium demonstrated in *Y-Z* cut planes using contour levels. (**C**) Shear rate on the top surface of the channel. (**D**) Schematic of sperm butterfly-shaped motion, with depiction of all the variables. The terms $\rho_\perp$ and $\rho'_\perp$ indicate the sperm perpendicular distance from both sidewalls, $\hat{e}_t$ is the unit vector along the sperm orientation, and θ and θ′ are the angles between the sperm orientation and the unit vector normal to the sidewalls. These variables are used in Eqs. 2 to 4. (**E**) Microscopic image of the sperm and the direction of flow. (**F**) Sperm path below the stricture for sperm with different velocities (40 to 80 μm/s). (**G**) Influence of Ω_{IN} on the sperm path. The value used as Ω_{IN} was experimentally measured as $0.12 \pm 0.06\ s^{-1}$. (**H**) Top: Initial angle of the sperm with the sidewall at the contact point for $\Omega_{IN} = -\Omega_{max}$, 0, and Ω_{max}, illustrated with red, green, and blue, respectively. Bottom: Time required for sperm to rotate upstream toward the stricture. (**I**) Total period (τ) required for sperm to depart from point A (C) and reach point C (A). The time elapsed in each mode is illustrated separately so that τ_f, τ_r, and τ_t correspond to the boundary, rotation, and transfer mode times.

width of the channel decreases. In Fig. 1B, the velocity profile of the fluid in four different cross sections is demonstrated using contour levels ($X = 0$, 25, 50, and 75 μm). According to the simulations, the maximum velocity field (125 μm/s) occurred in the stricture of the channel ($X = 0$) and decreased to as low as 20 μm/s at $X = 300$ μm. To use these numerical results for simulating the rheotactic behavior of the sperm, we extracted the shear rate of the fluid on the top surface of the chip in the $\hat{z}$ direction using $\gamma_z = \frac{\partial v}{\partial z}$, as shown in Fig. 1C, in which v is sperm medium velocity field. Moreover, we found the shear rate near the sidewalls using $\gamma_n = \frac{\partial v}{\partial n}$, in which n is the perpendicular distance from the sidewall. $\hat{n}$, the unit vector perpendicular to the sidewalls, is depicted in Fig. 1D.

To simulate the swimming path of the sperm, we assumed that the sperm location was influenced by its propulsive velocity, the velocity field of the medium, and the velocity components induced by the hydrodynamic interactions with the sidewalls. These hydrodynamic interactions with the sidewalls are created from the contribution of the microswimmer to the fluid flow in the presence of boundaries. Consequently, the time derivative of the sperm location can be written using the following equation

$$\frac{d\vec{r}}{dt} = \vec{v}_{\text{sperm}} + \vec{v}_{\text{fluid}} + \frac{d\vec{\rho}_\perp}{dt} + \frac{d\vec{\rho}'_\perp}{dt} \quad (1)$$

in which $\vec{v}_{\text{sperm}}$ is the sperm propulsive velocity in the absence of the sidewalls and fluid flow, and $\vec{v}_{\text{fluid}}$ is the sperm medium velocity field within the microfluidic channel at $Z = h - \delta$, where h is the channel height and the δ value reported for sperm is ~10 μm (fig. S1). The two rightmost terms in Eq. 1 represent the drift velocity components induced by hydrodynamic interactions of the sperm with the sidewalls, and the terms $\rho_\perp$ and $\rho'_\perp$ are the perpendicular distances of the sperm from the sidewalls, as shown in Fig. 1D.

To determine the drift velocities induced by the hydrodynamic interactions at large distances from the sidewalls ($\rho_\perp$ or $\rho'_\perp > 50$ μm), we first calculated the contribution of the microswimmer to the fluid flow

by using a dipole pusher swimmer model proposed by Berke *et al.* (*27*). In the dipole pusher swimmer model, the flow produced by the swimmer is modeled by two forces with equal magnitudes and opposite directions that act on two points in the fluid with a distance equal to the swimmer length. For a point force, the solution of the Stokes equation is its Green's function, known as "Stokeslet," and the solution for a dipole swimmer is thus Stokes doublet. For the sake of simplicity, we then used the image method to consider the existence of the sidewalls and satisfy the no-slip boundary condition on the sidewall. By neglecting the reflection of each image system on the other sidewall, we found the hydrodynamic interaction terms (drift velocities) to be inversely correlated to the perpendicular distance of the sperm from the sidewalls, as described by

$$\frac{d\vec{\rho}_{\perp}}{dt} = -\frac{3P}{64\pi\eta{\rho_{\perp}}^3}(1-3\cos^2\theta)\vec{\rho}_{\perp} \quad (2)$$

$$\frac{d\vec{\rho'}_{\perp}}{dt} = -\frac{3P}{64\pi\eta{\rho'_{\perp}}^3}(1-3\cos^2\theta')\vec{\rho'}_{\perp} \quad (3)$$

in which P is the dipole strength of the sperm, η is the viscosity of the sperm medium, and θ and θ' are the angles between the swimming direction of the sperm and the sidewalls. On the basis of Eqs. 2 and 3, when $|\cos\theta| \leq 1/\sqrt{3}$, the sidewalls repel the sperm; otherwise, they attract it. To calculate the vertical distance of the sperm from the sidewalls, we found the microswimmer's minimum distance from the sidewalls at each point simulated in the channel.

However, the dipole swimmer model as a far-field approximation is not accurate at distances closer to the wall ($\rho_{\perp}$ or $\rho'_{\perp} < 50$ μm). Therefore, we further developed a model based on the lubrication approximation (fig. S2) to obtain the drift velocities imposed on the swimmer at near-wall conditions (see the Supplementary Materials for more details). On the basis of our model, the drift velocities imposed on the swimmer at near-wall conditions can be described by

$$\frac{d\vec{\rho}_{\perp}}{dt} = \frac{6\eta dV\sin(\theta)}{\xi_n L\cot^2(\theta)}\left(\frac{2L\cos(\theta)}{2\rho_{\perp}+L\cos(\theta)} + ln\left(\frac{\rho_{\perp}}{\rho_{\perp}+L\cos(\theta)}\right)\right) \quad (4)$$

$$\frac{d\vec{\rho'}_{\perp}}{dt} = \frac{6\eta dV\sin(\theta')}{\xi_n L\cot^2(\theta')}\left(\frac{2L\cos(\theta')}{2\rho'_{\perp}+L\cos(\theta')} + ln\left(\frac{\rho_{\perp}}{\rho'_{\perp}+L\cos(\theta')}\right)\right) \quad (5)$$

where V is the magnitude of the sperm velocity, L is the length of the sperm tail, ξ_n is the friction coefficient of the sperm medium in the normal direction, and d is the sperm width and considered to be 5 μm.

We considered the magnitude of the $\vec{v}_{\text{sperm}}$ as a constant value over time, since the sperm energy loss was not considered in this paper. However, sperm swimming direction evolves with time and the sperm angular velocity is affected by its fluid mechanical response to an external fluid, intrinsic rotation, and response to the sidewalls (i.e., hydrodynamic interactions). Therefore, and on the basis of the superposition principle, the angular velocity of the sperm at each point between the sidewalls can be described by

$$\vec{\Omega}_{\text{sperm}}(\vec{r},t) = (-\Omega_{\text{RH}} - \Omega_{\text{IN}} - \Omega_{\text{HI}})\hat{z} \quad (6)$$

in which Ω_{RH} is the rheotactic angular velocity caused by the response of the sperm to the fluid flow. Bukatin *et al.* (*20*) have observed that under a flow reversal condition, half of the sperm make a left-hand U-turn, whereas the other half make a right-hand turn based on their initial alignment. We thus assume that the sperm rotation toward the left- and right-hand sides obeys a similar rate (we examine the accuracy of this assumption in the following experimental sections). This sperm rotation rate has been described with Eq. 7 [by Tung *et al.* (*21*) and Bukatin *et al.* (*20*)]

$$\Omega_{\text{RH}} = \lambda\gamma_z \sin\psi(\vec{r},t) \quad (7)$$

in which λ is a dimensionless constant related to the asymmetry in the sperm geometry, γ_z is the shear rate in the vicinity of the top surface along the $-\hat{z}$ direction (Fig. 1C), and as shown in Fig. 1E, $\psi(\vec{r},t)$ is the angle between the direction of the sperm movement and the velocity field, which can be obtained by $\psi(\vec{r},t) = \cos^{-1}\left(\frac{\vec{v}_{\text{sperm}}\cdot\vec{v}_{\text{fluid}}}{|\vec{v}_{\text{sperm}}|\cdot|\vec{v}_{\text{fluid}}|}\right)$.

The intrinsic rotation (Ω_{IN}) is the angular velocity created from asymmetry in the beating pattern of the sperm tail. The sperm flagellum does not feature a sine wave with a single frequency and phase. Rather, the mechanical wave produced by the sperm tail encompasses sine waves with different frequencies and initial phases. Consequently, the sperm tail beating pattern is asymmetric, which yields to an intrinsic rotation (see the "Intrinsic angular velocity" section of the Supplementary Materials) (*14*). This rotation can be modeled by an intrinsic angular velocity that is described by Eq. 8

$$\Omega_{\text{IN}} \propto v_{\text{propulsion}}\left(\frac{\xi_t}{\xi_n}\right)\frac{y_n}{L^2}\cos(\phi) \quad (8)$$

in which ξ_t is tangential friction coefficient of the sperm medium, y_n is the amplitude of the nth harmonic of the sperm tail, and ϕ is the phase difference between the main sine wave and the nth harmonic. Since ϕ is an arbitrary parameter, Ω_{IN} can vary from $-\Omega_{\max}$ to $\Omega_{\max}$, which means that its rotation can be either counterclockwise or clockwise. To experimentally measure the intrinsic angular velocity (movie S1 and figs. S3 and S4), we extracted the trajectories of 28 sperm trapped in an area with no background fluid flow. The majority of the sperm were moving clockwise, and the value that we measured for those sperm was $\langle\Omega_{\text{IN}}\rangle = 0.12 \pm 0.06\ \text{s}^{-1}$. Accordingly, the absolute value of the intrinsic angular velocity in all simulations was assumed to be less or equal to $\langle\Omega_{\text{IN}}\rangle$ ($|\Omega_{\text{IN}}| \leq \langle\Omega_{\text{IN}}\rangle = \Omega_{\max}$).

To find the rotation induced in the swimmer caused by the hydrodynamic interaction, we used the dipole swimmer model for distances adequately far from the sidewalls, while for near-wall conditions, the lubrication theory was used. Therefore, the total rotation caused by the presence of the sidewalls can be written out as

$$\Omega_{\text{HI}}(\vec{r},t) = \Omega^1{}_{\text{HI}}(\vec{r},t) + \Omega^2{}_{\text{HI}}(\vec{r},t) \quad (9)$$

where $\Omega^1{}_{\text{HI}}$ and $\Omega^2{}_{\text{HI}}$ are the contribution of each sidewall in the induced rotation. If the distance of the swimmer from a sidewall is

large enough ($\rho_\perp > 50$ μm), then the sperm rotation induced by that wall can be described by

$$\Omega^1{}_{HI}(\vec{r},t) = -\frac{3P\cos\theta\sin\theta\,(3+\cos^2\theta)}{128\eta\rho_\perp{}^3} \quad (10)$$

as proposed by Berke *et al.* (*27*). Otherwise ($\rho_\perp < 50$ μm), on the basis of the model explained in the Supplementary Materials (lubrication approximation), we used eq. S13 to describe the rotation. By calculating the rotation induced by the other sidewall using a similar manner, the rotation induced on the sperm by hydrodynamic interactions was reflected in the calculations.

As sperm is a large microswimmer (in comparison to bacteria and other swimming particles), and the role of noisy fluctuations is important for swimmers with size much smaller than sperm, we neglect the white zero-mean Gaussian noise in rotation of the sperm head (*12*). Last, we can write the time derivative of the sperm swimming direction $\hat{e}_t(\vec{r},t)$ as the outer product of this unit vector with the angular velocity vector of the sperm

$$\dot{\hat{e}}_t(\vec{r},t) = \vec{\Omega}(\vec{r},t)\times\hat{e}_t(\vec{r},t) \quad (11)$$

For $\Omega_{IN} = 0$ and the initial sperm orientation parallel to the sidewall, the trajectory calculated for the sperm with different velocities is presented in Fig. 1F. Since the shear rate within the stricture is too high for sperm to pass, the swimmer detaches from the sidewall at the vicinity of the stricture and is swept away by the flow until it reaches the other sidewall. The sperm trajectory depicted in Fig. 1F shows that the location of the initial contact point of the sperm, and this sidewall is not linearly related to the sperm velocity. That is, as the sperm velocity declines, the sperm are increasingly carried away by the fluid flow. To demonstrate the impact of intrinsic rotation on the sperm locomotion, the trajectories of the swimmers with velocities of 40, 50, and 60 μm/s are also depicted in Fig. 1G for $|\Omega_{IN}| \le \Omega_{max}$. As can be seen, the effect of intrinsic rotation is more substantial on slower sperm (40 μm/s), whereas the increase/decrease in location of the initial contact point caused by Ω_{IN} is smaller for faster sperm (60 μm/s).

Upon arrival to the opposing sidewall, the shear rate along $\hat{n}$ (i.e., γ_n) starts rotating the sperm upstream. Depending on the angle between the sperm orientation and the sidewall at the contact point (Fig. 1H, top), and the sperm velocity, which determines the location of the contact point, the rotation time will vary (Fig. 1H, bottom). In Fig. 1H (top), the initial angle of the sperm with the sidewall is depicted for different velocities, with the red, green, and blue curves corresponding to $\Omega_{IN} = -\Omega_{max}$, 0, and Ω_{max}, respectively. The evolution of the angle between the sperm orientation and the sidewall at the contact point is determined by Eq. 5, in which γ_z is replaced with γ_n and the rotation rate obtained from lubrication theory. Therefore, the time required for the sperm to reorient itself upstream is the time required to decrease its angle with the sidewall from α_0 to $\delta/L \sim \frac{\pi}{20}$ (fig. S1). After the upstream orientation, the sperm starts following the sidewall. This boundary movement is simply determined by the shear rate along the $\hat{n}$ direction multiplied by δ subtracted from its propulsive velocity. Last, the total time required for sperm to return to its initial X coordinate ($A \rightarrow C$), τ is shown in Fig. 1I for different sperm velocities. τ includes the time required for sperm to transfer from one sidewall to the other (τ_t), rotate upstream at the contact point B/D (τ_r), and follow the boundary in the stricture direction (τ_f). The time required for sperm to return to the initial X and Y coordinates is $2 \times \tau$.

On the basis of the simulation, sperm movement below the stricture—i.e., the hydrodynamic barrier—is composed of three different modes: (i) transfer mode, in which the sperm detaches from the sidewall, becomes swept back by the flow, and reaches the opposing sidewall; (ii) rotation mode, which involves sperm rotation around its head (i.e., the pivot) at the contact point; and (iii) boundary swimming mode. When sperm motion begins at point A, its initial orientation is parallel to the sidewall, as can be seen in Fig. 1D. The high shear rate at the mouth of the stricture causes the sperm to be

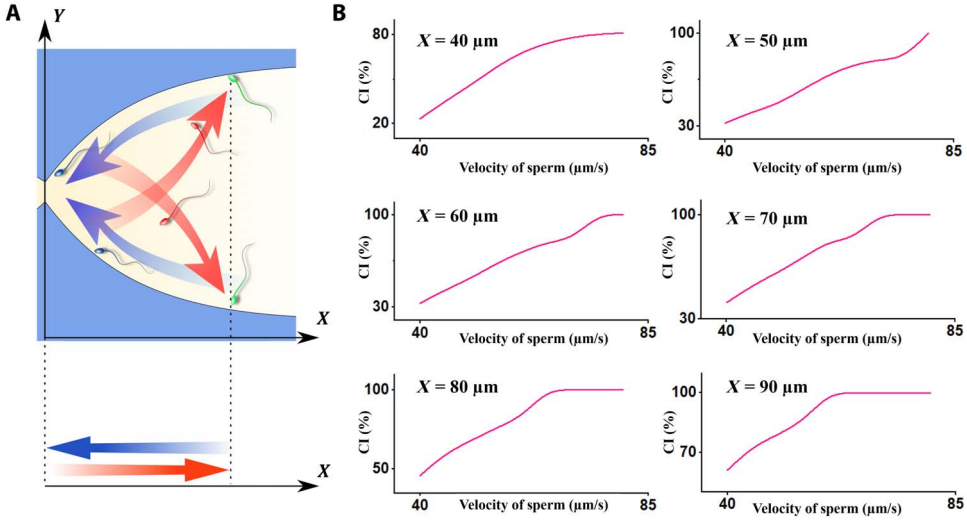

Fig. 2. Sperm motion modes and the CI. (**A**) Schematic of sperm motion in different modes, including transfer, rotation, and boundary swimming modes, illustrated in red, green, and blue, respectively. The sperm projection in the *X* direction demonstrates a periodic motion, on which we based the CI. (**B**) The CI for sperm slower than a particular velocity drops depending on the value of *a*.

swept back to point B on the opposing sidewall (i.e., transfer mode), at which point it stops moving perpendicular to the BC sidewall and starts rotating counterclockwise (i.e., rotation mode). By rotating near the wall, the sperm orients its direction parallel to the BC sidewall and begins moving along it in the direction of the stricture (i.e., boundary swimming mode). Upon arrival at point C, it detaches from the sidewall (similar to point A) because of the high shear rate of the structure and begins swimming toward the AD sidewall again. This periodic motion takes on a butterfly-shaped path (A → B → C → D → A) and continues until the sperm has no more energy to swim.

For a given angle between the two sidewalls (β), only sperm with velocities in a specific range can move in butterfly-shaped paths (fig. S5). The upper limit of this range is determined by the shear rate in the stricture. The lower limit of the range, however, is determined by two conditions: (i) proximity to the stricture, and (ii) return-ability conditions. The proximity condition determines the velocity of all sperm that can become proximate to the stricture, while the return-ability condition means that at points B and D, the shear rate is adequate to reorient sperm toward upstream. Since the shear rate outside the stricture decreases, depending on the angle, sperm can get close to the stricture. By defining the proximity zone as $x < 5$ μm (the average size of the bull sperm head), for β ~ 80°, all the sperm with velocities between ~30 and 80 μm/s were able to become proximate to the stricture. By considering the return-ability condition, we observed that among the sperm with velocities in this range, the fluid flow can reorient only sperm with velocities higher than 40 μm/s at point B (and D) in Fig. 1D. The angle between the swimming direction and the sidewall at point B (and D) for sperm with motilities slower than 40 μm/s becomes greater than 90°, and the shear rate in these points is inadequate to reorient the sperm upstream. Consequently, sperm slower than 40 μm/s follow the boundary in the downstream direction.

Given the similarity between this stricture to the junctions of the sperm's path toward the site of fertilization, and the direction of the fluid flow, which simulates the mucus outflux within the tract, the final goal of the sperm in this situation is to pass through the stricture and advance toward the site of fertilization, or at least to maintain its location nearby the stricture. Since it is known that no sperm with velocities in the range of 40 to 80 μm/s can pass through the stricture, we defined the ability of the sperm to remain close to the stricture mouth as a competition index (CI). Since the main path of the sperm toward the fertilization site is in the $-\hat{x}$ direction, we projected the sperm periodic motion onto the x axis, as can be seen in the schematic of sperm motion in Fig. 2A. Given the total period of the sperm motion ($T = \tau$), and neglecting the translational diffusivity of the sperm (*28*), the probability of the sperm to be closer to the stricture than at $x = a$ can be defined as

$$\mathrm{CI} = F_X(x) = pr\{X \le x = a\} = \int_0^a dx P(x,t) = \int_0^{T_a} \frac{dt}{T} + \int_{T'a}^{T} \frac{dt}{T} = \frac{T_a + T - T'_a}{T} \quad (12)$$

in which T_a and T'_a are the times at which $x = a$ (Fokker-Planck equation in the Supplementary Materials). We calculated the CI for different values of a as a function of sperm velocity, the results of which are shown in Fig. 2B.

We also experimentally observed the butterfly-shaped motion described by the simulation in our microfluidic device. To observe all the sperm with motilities in the range of 40 to 80 μm/s swim in butterfly-shaped paths and demonstrate rheotactic behavior and to perform comprehensive experimental characterization of this swimming behavior, we designed the flow rate such that the shear rate of the stricture was $8s^{-1}$. This shear rate is high enough to prevent all the sperm from passing through. Furthermore, given the shear rate within the stricture was $8s^{-1}$, the stricture mouth angle was chosen to be equal to ~ 80 ° so that all the sperm with motilities in the range of 40 to 80 μm/s were able to exhibit rheotactic behavior and thus swim in a butterfly-shaped path. Although the butterfly-shaped swimming path was also discernible at different stricture mouth angles, the motility range of the sperm that exhibit such a motion was smaller than 40 to 80 μm/s, which lowers the comprehensiveness of our study. The butterfly-shaped motion of a bull sperm with a velocity of 54 μm/s is demonstrated in Fig. 3 (A and B). Figure 3A is a combined image of the sperm location at 23 different frames, and Fig. 3B is the corresponding schematic of the sperm swimming pattern based on Fig. 3A for better visualization. As can be seen, the butterfly-shaped path is left-right symmetric, confirming the assumption that we made regarding the sperm featuring a similar rotation toward the right- and left-hand sides. This left-right symmetry is also in total agreement with previous observations reported by Bukatin *et al.* (*20*). To extract the sperm trajectories, we acquired videos of the device, as shown in movie S2, and tracked the sperm movement over the elapsed time (i.e., 3 to 20 periods). Using MATLAB R2017a, we tracked 44, 35, and 51 sperm heads displaying different motilities to elucidate the trajectories of each microswimmer in three different sperm samples. Figure 3C displays the motion of a single sperm at two different periods, in which the shape of the swimming path remained relatively constant over the elapsed time (t_{blue} = 0 − 6.24 s, t_{red} = 38.14 − 44.11 s). The motion of the sperm and its butterfly-shaped path, as can be seen in Fig. 2C, is similar to the results obtained by simulations presented in Fig. 1F.

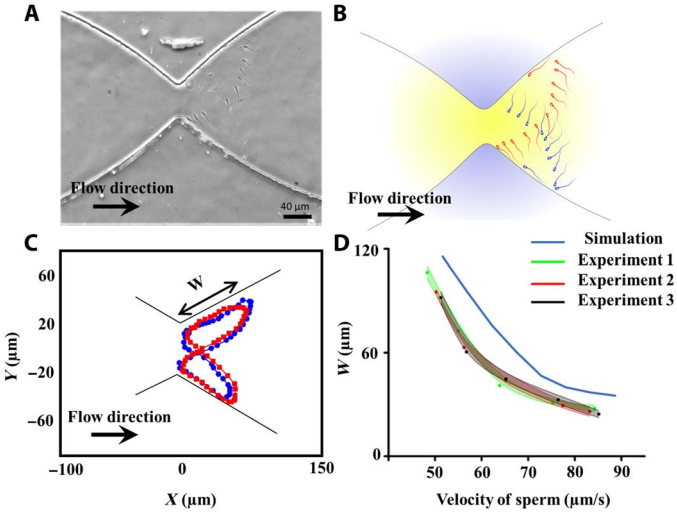

Fig. 3. Observation of the butterfly-shaped swimming path and withdrawal distance of sperm below a stricture. (**A**) Butterfly-shaped path extracted for a sperm with a velocity of 57 μm/s. (**B**) Schematic of the butterfly-shaped path based on the experimental results obtained in (A) for better visualization. (**C**) Trajectory of the sperm during two different periods to illustrate the consistency of the butterfly-shaped path over time. *W* is the withdrawal distance of the sperm. (**D**) Experimental values of the withdrawal distance extracted from 130 sperm with different velocities from three different samples in comparison with values expected by simulations.

To confirm the results obtained from the simulations, we experimentally measured the distance between the sperm-sidewall contact points (B and D) and detachment points (A and C), i.e., the "withdrawal distance," for sperm with different velocities. As shown in Fig. 3D, the increasing velocity of the sperm led to a decay in the withdrawal distance (W). According to simulation- and experimental-based results, the decay in the withdrawal distance is exponentially correlated to the sperm velocity. That is, the difference in the withdrawal distances of two sperm is not only related to difference in the velocity of those swimmers—the velocity of the sperm plays a determinative role as well. For instance, on the basis of experimental data, the mean withdrawal distances measured for sperm with velocities of ~75 and ~85 μm/s were 39.1 and 28.2 μm, respectively. However, for two slower sperm (~55 and ~65 μm/s) with the same difference in velocity, the corresponding withdrawal distances were 74.6 and 51.3 μm. This dependency of the sperm swimming path with the velocity of the sperm suggests that swimmers with higher velocities move closer to each other, and their corresponding CIs are closer in comparison than slower sperm.

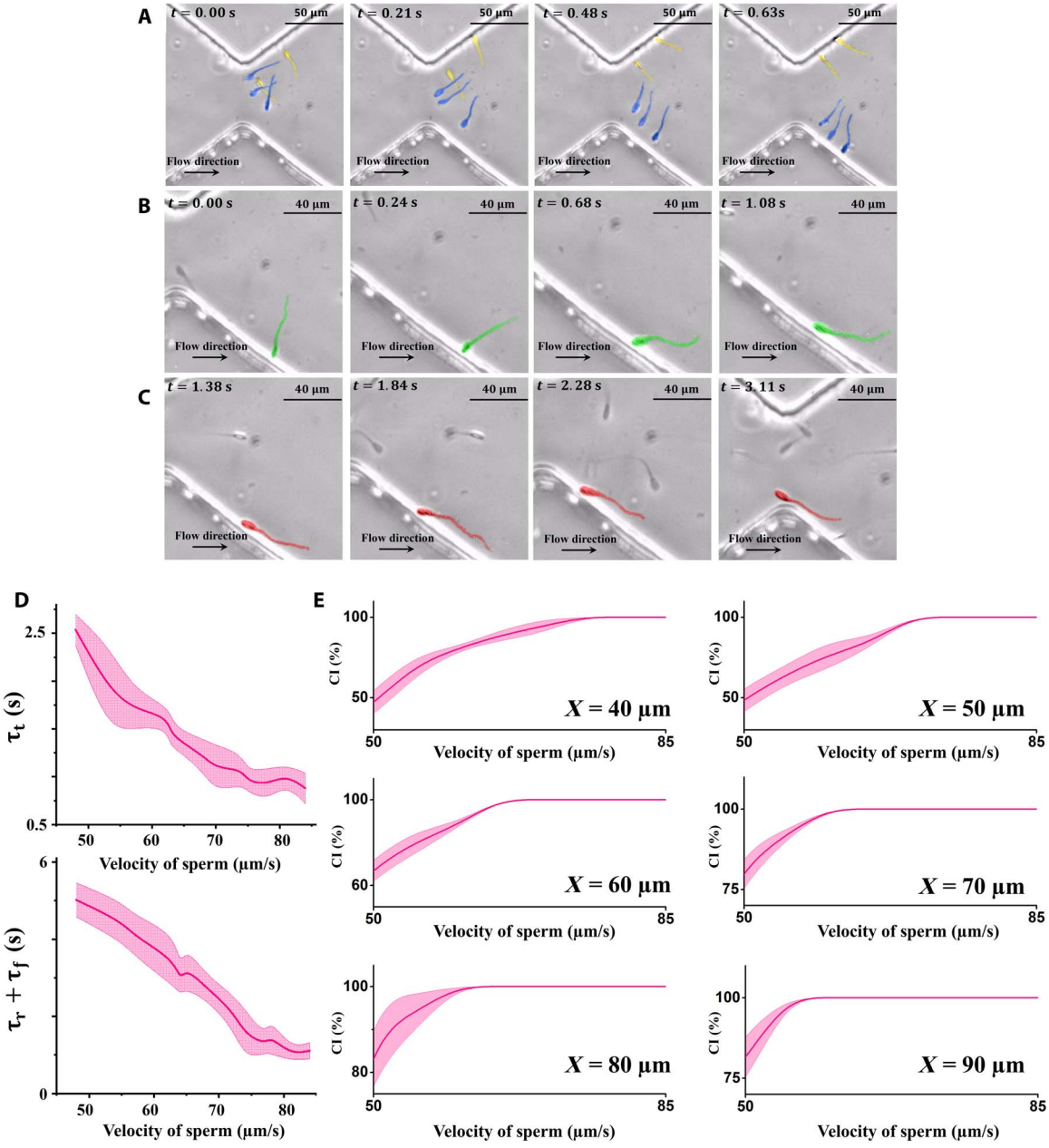

Fig. 4. Experimentally measured times of the different swimming modes (i.e., transfer, rotation, and boundary swimming) and CI calculated for sperm. (**A**) Images of sperm (blue and yellow) moving in the transfer mode. (**B**) A single sperm (green) in the rotation mode, reorienting upstream. (**C**) A sperm (red) in the boundary swimming mode begins following the sidewall. (**D**) The times required for sperm to transfer (τ_t), rotate (τ_r), and follow the boundary (τ_f) were experimentally measured for 120 sperm. Since the rotation and the boundary swimming times overlapped, their sum ($\tau_r + \tau_f$) was reported and measured. (**E**) For a given a, as the velocity of the sperm decreases, its likelihood to maintain its X coordinate closer than a decays.

In addition to withdrawal distance, we also measured the elapsed time taken for sperm to move in the transfer, rotation, and boundary swimming modes. The images acquired from sperm at different time frames and modes are presented in Fig. 4. In the pictures shown in Fig. 4A, five sperm are moving in the transfer mode, in which three of them (colored blue) are departing the upper sidewall and moving toward the bottom sidewall. Likewise, the remaining two sperm (yellow-colored) are departing the bottom sidewall toward the upper sidewall. In Fig. 4B, a moderately motile sperm with a velocity of ~59 μm/s can be seen beginning to rotate upstream because of the shear rate along the normal direction of the sidewall. Later on, this sperm swims along the boundary of the sidewall until it reaches the stricture, as can be seen in Fig. 4C. These experimental observations of sperm movement thus help confirm our simulated derivations of the three different sperm swimming modes.

The corresponding elapsed times of each mode (τ_t, τ_r, and τ_f) are presented in Fig. 4D. Since the rotation and boundary swimming times somewhat overlap, especially for highly motile sperm, we combined the amount of time required for each of these modes into a single measurement ($\tau_r + \tau_f$). Using these times, we measured the CI from experimental data of sperm featuring different velocities for different values of a (Fig. 4E). At a = 40 μm, the CI measured for sperm with velocities higher than 78 μm/s was close to 100%, which means that these sperm were always closer than 40 μm to the stricture. For velocities below 78 μm/s, the CI decays, with the CI for the slowest sperm (v = 48 μm/s) being 14.3%. In the case of a = 50 μm, the range of velocity for sperm with a CI of 100% expands, and sperm faster than 72 μm/s are always closer than 50 μm to the stricture.

The similarity between human and bovine sperm in terms of the shape and swimming mechanism suggests that the motion of the human sperm below the stricture is similar to that of bovine sperm. We also experimentally observed human sperm motion below the stricture (movie S3), and as was expected, the butterfly-shaped swimming path was seen in human sperm as well (fig. S6). Moreover, the human sperm motion in the transfer, rotation, and boundary swimming modes is also demonstrated in fig. S7, which confirms the similarity between human and bull sperm locomotion strategies.

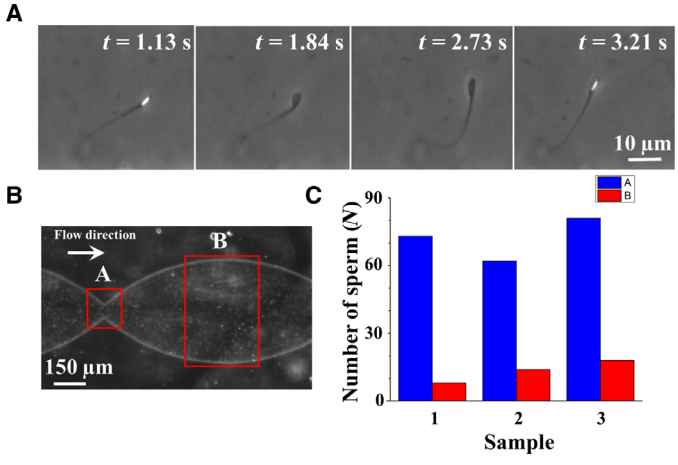

Fig. 5. Accumulation of sperm below the stricture and the twinkling effect. (**A**) Phase-contrast microscopy leads to twinkling of the bull sperm. (**B**) Low-magnification image of our device with a concentrated sample injected. Zones A and B are indicated in the image. (**C**) The number of live sperm in each zone for three different samples was counted manually to confirm the accumulation of the sperm.

Accumulation of sperm near the stricture

In agreement with previous studies done in the absence of fluid flow (*29*, *30*), the butterfly-shaped motion (due to the sperms' ability/tendency to swim counter to the flow and parallel to the sidewalls) also leads to the accumulation of sperm near the stricture, which could be interpreted as a mechanism used by the sperm to resist against the fluid flow. Despite dead and nonmotile sperm being carried away by the flow, motile sperm maintained their proximity to the stricture, and thus, their likelihood to pass through it is high. To observe this accumulation phenomenon, we observed the microfluidic device using low-magnification phase-contrast microscopy (movie S4) (*31*). To assess the abundancy of the sperm, we took advantage of the twinkling effect observed in the motile bull sperm due to the paddle-shaped head of the microswimmers, in which the side of the sperm flashes bright under the imaging conditions, while the head's top and bottom faces appear dark (Fig. 5A). Zone A of Fig. 5B, which describes the area of the device that includes the stricture, features more twinkling, whereas zone B, which includes the wider region of the channel, twinkles less, as can be seen in movie S4. On the basis of this evidence, we can conclude that more sperm accumulate near the stricture. To validate this twinkling effect–based result, we manually counted the total number of motile sperm swimming in zones A and B at high magnification, the results of which are shown in Fig. 5C for three samples. With this method as well, we observed that the number of sperm that accumulate below the stricture is greater than that of zone B. This accumulation below the stricture demonstrates sperm resistivity against the flow, which leads to persistence upon advancing toward the egg, thus maintaining the chance of fertilization.

Gate-like role of the stricture

The height of the hydromechanical barrier (i.e., the shear rate within the stricture) determines the threshold motility that sperm must have to overcome and pass through the stricture. To experimentally observe the gate-like role of the stricture, we decreased the sperm medium injection flow rate and, consequently, the shear rate within the stricture to 7.98 s^{-1}. As a result, the sperm with the highest motility (v = 84.2 μm/s, sperm number 1) could resist against the flow within the stricture, as can be seen in Fig. 6A and movie S5. Meanwhile, all the sperm with lower velocities (sperm numbers 2 to 6) maintained their location below the barrier by periodically moving between the sidewalls. Under these conditions, sperm number 1 is almost static in the observer frame in the $\hat{x}$ direction, as neither the shear rate of the flow nor the sperm's motility can overcome the other. By further decreasing the shear rate of the stricture to 7.16 s^{-1}, eventually, sperm number 1 can overcome the barrier and advance toward the next compartment, as can be seen in Fig. 6B and movie S5. Meanwhile, all other sperm with lower velocities accumulate below the barrier in a hierarchical manner, i.e., sperm with higher velocities remain closer to the stricture and slower sperm are swept further back by the flow. To characterize the gate-like role of the stricture in motility-based selection of sperm, we gradually decreased the flow rate (thus the shear rate of the stricture) and measured the velocity of the sperm that passed through the stricture, which we call the "threshold sperm velocity." The threshold sperm velocity with regard to the shear rate within the stricture is depicted in fig. S8, which demonstrates a linear correlation (P = 0.01) between the threshold sperm velocity and the

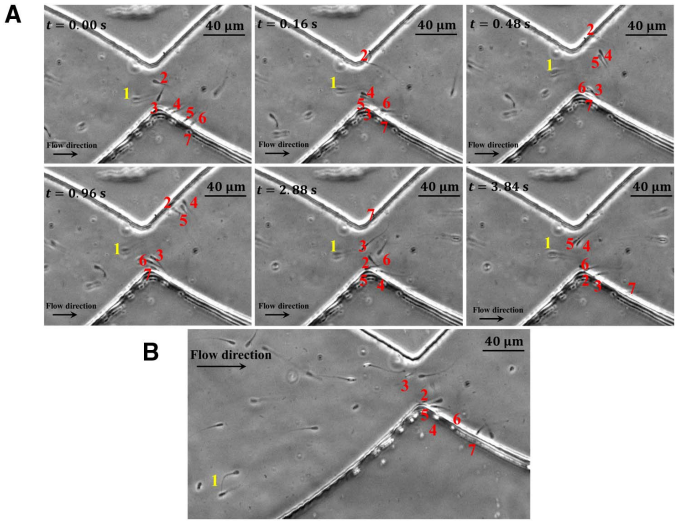

Fig. 6. Gate-like role of the stricture. (**A**) Sperm number one is able to resist against the shear rate in the stricture, and therefore, it has approximately no movement in the *–X* direction. The other sperm (numbers 2 to 7) move in butterfly-shaped paths, but they cannot pass through the junction. Hierarchical swimming is discernible, and sperm with higher velocity are closer to the stricture and to each other. (**B**) A small decrease (7.98 to 7.16 s^{-1}) in the injection flow rate led to sperm number 1 advancing and entering the adjacent compartment. Meanwhile, the slower sperm continue to swim on the butterfly-shaped path below the stricture.

shear rate of the stricture. The similarity between the geometry of the stricture and the junctions within the female reproductive tract suggests that the gate-like selective behavior of this microfluidic stricture can mimic the potential role of junctions in motility-based selection for sperm during fertilization (*26*).

CONCLUSION

The response of sperm to fluid flow and their inclination to follow solid boundaries lead to the accumulation of sperm below the stricture opening inside a microfluidic design. The accumulated sperm form a hierarchy, in which swimmers with higher motilities are closer together near the stricture mouth while slower sperm remain further apart away from the stricture. Using numerical simulations and experimental observations, we can quantitatively show that this hierarchical structure imposes competition among the sperm, with the fiercest competition occurring among highly motile microswimmers in comparison with the slower sperm. Moreover, depending on the shear rate within the stricture, sperm with velocities higher than a threshold value can pass through the stricture, whereas sperm slower than the threshold accumulate below the stricture. This gate-like behavior shows that sperm location is maintained near the stricture until the shear rate within the stricture decreases; thus, the chance of the sperm to pass through the stricture is maximized.

This gate-like behavior of the stricture suggests a motility-based selection mechanism that may potentially be used by the female reproductive tract to select for sperm with the highest motility. Moreover, since we observed sperm accumulation below the stricture when the shear rate was not sufficiently low enough for the sperm to pass through the stricture, and given the fluid mechanical similarity between the stricture in the microchannel and junctions of the female reproductive tract, this investigation suggests that in these geometries, highly motile sperm are more likely to pass through the fluid mechanical barriers and advance toward the fertilization site.

MATERIALS AND METHODS

Bull and human sperm samples

All the experiments were performed with four bull sperm samples frozen in 250-μl straws that were purchased from Genex Cooperative (Ithaca, NY). Semen from two of the bulls was frozen in a milk-based extender, and semen from the other two bulls was frozen in an egg yolk–based extender at a concentration of 100 million sperm/ml. Frozen straws were thawed in a 37°C water bath. Then, the live sperm were separated from the dead sperm using a density gradient method (*23*). The separated sample was then diluted 1:3 using TALP (Tyrode's albumin lactate pyruvate) medium. The viscosity of the bull sperm sample after the dilution was 0.87 mPa·s at T = 37°C.

Fresh human sperm samples were provided by Weill Cornell Medicine in accordance with the Weill Cornell Medicine Institutional Review Board (IRB) guidelines. An approved IRB consent form was used to prospectively recruit patients interested in participating in this study. The original concentration of the human sperm sample was 46 million sperm/ml. All experiments carried out on human samples diluted 1:3 with TALP medium at T = 37°C. The viscosity of the human sample after the dilution was 0.94 mPa·s. The TALP recipe was as follows: NaCl (110 mM), KCl (2.68 mM), NaH_2PO_4 (0.36 mM), $NaHCO_3$ (25 mM), $MgCl_2$ (0.49 mM), $CaCl_2$ (2.4 mM), Hepes buffer (25 mM), glucose (5.56 mM), pyruvic acid (1.0 mM), penicillin G (0.006% or 3 mg/500 ml), and bovine serum albumin (20 mg/ml).

Device fabrication and injection systems

We used conventional soft lithography (*32*) to fabricate the microfluidic device out of polydimethylsiloxane. We used conventional soft lithography to fabricate the microfluidic device out of polydimethylsiloxane. Syringe pumps (Chemyx Fusion 200) were used to control the flow rate of the sperm medium at different injection rates of 0 to 2 ml/hour. Using the syringe pump, we were able to manipulate the input pressure and the injection rate. Furthermore, to obtain very low flow rates (0 to 0.6 ml/hour), we used gravity to inject the sample, in which case the flow rate was controlled by changing the height of the sample container.

Image and video acquisition

Images and videos were acquired at 25 frames/s using phase-contrast microscopy with a 10× objective and a digital Neo complimentary metal-oxide semiconductor camera. During the experiments, the microfluidic chip was kept on a heated microscope stage (Carl Zeiss, at 37°C). The average path velocity of the sperm (also called VAP in computer-assisted sperm analysis systems) was determined using ImageJ (version 1.51j8) and MATLAB (version R2017a) software by measuring the average distance between the center of the sperm head in each frame divided by the time elapsed.

Simulation software

The layout of the microfluidic device was imported into COMSOL MULTIPHYSICS (version 5.2) simulation software. Using the laminar fluid module in a stationary mode, we solved the Navier-Stokes (Eq. 13)

and conservation of mass (Eq. 14) equations with a no-slip boundary condition at the sidewalls (*33*)

$$\rho(v.\nabla v) = -\nabla p + \nabla.\mu(\nabla v + (\nabla v)^{T}) \quad (13)$$

$$\nabla.v = 0 \quad (14)$$

in which v denotes the velocity field, ρ is the density of the sperm medium, p is pressure, and μ is the dynamic viscosity. To numerically solve the sperm equations of motion, MATLAB (version R2017a) and an explicit Runge-Kutta method [i.e., the Dormand-Prince pair (*34*)] was used.

SUPPLEMENTARY MATERIALS

Supplementary material for this article is available at http://advances.sciencemag.org/cgi/content/full/5/2/eaav2111/DC1

Fig. S1. Sperm tilted orientation in the boundary swimming mode.
Fig. S2. Schematic of the model used for lubrication theory.
Fig. S3. Sperm intrinsic angular velocity and curvature.
Fig. S4. Intrinsic angular velocities measured for sperm when the external flow was zero.
Fig. S5. Impact of stricture mouth angle on the butterfly-shaped motion of sperm.
Fig. S6. Butterfly-shaped motion of human sperm.
Fig. S7. Transfer, rotation, and boundary swimming modes with corresponding times for human sperm.
Fig. S8. Threshold sperm velocity versus shear rate of the stricture.
Movie S1. Sperm intrinsic rotation.
Movie S2. Bovine sperm swimming on butterfly-shaped paths.
Movie S3. Human sperm swimming on butterfly-shaped paths.
Movie S4. Accumulation of the sperm below the stricture.
Movie S5. Gate-like role of the stricture.
References (*35*–*40*)

REFERENCES AND NOTES

1. D. Tulsiani, *Introduction to Mammalian Reproduction* (Springer Science & Business Media, 2012).
2. S. S. Suarez, A. A. Pacey, Sperm transport in the female reproductive tract. *Hum. Reprod. Update* **12**, 23–37 (2006).
3. T. R. Birkhead, A. P. Møller, *Sperm Competition and Sexual Selection* (Academic Press, 1998).
4. X. Sun, Female reproductive system, in *Well-Differentiated Malignancies: New Perspectives* (Humana Press, Springer Science & Business Media, 2015), pp. 67–98.
5. S. S. Suarez, Mammalian sperm interactions with the female reproductive tract. *Cell Tissue Res.* **363**, 185–194 (2016).
6. U. B. Kaupp, J. Solzin, E. Hildebrand, J. E. Brown, A. Helbig, V. Hagen, M. Beyermann, F. Pampaloni, I. Weyand, The signal flow and motor response controling chemotaxis of sea urchin sperm. *Nat. Cell Biol.* **5**, 109–117 (2003).
7. S. Publicover, C. V. Harper, C. Barratt, $[Ca^{2+}]_i$ signalling in sperm—Making the most of what you've got. *Nat. Cell Biol.* **9**, 235–242 (2007).
8. T. Strünker, N. Goodwin, C. Brenker, N. D. Kashikar, I. Weyand, R. Seifert, U. B. Kaupp, The CatSper channel mediates progesterone-induced Ca^{2+} influx in human sperm. *Nature* **471**, 382–386 (2011).
9. L. Alvarez, L. Dai, B. M. Friedrich, N. D. Kashikar, I. Gregor, R. Pascal, U. B. Kaupp, The rate of change in Ca^{2+} concentration controls sperm chemotaxis. *J. Cell Biol.* **196**, 653–663 (2012).
10. J. F. Jikeli, L. Alvarez, B. M. Friedrich, L. G. Wilson, R. Pascal, R. Colin, M. Pichlo, A. Rennhack, C. Brenker, U. B. Kaupp, Sperm navigation along helical paths in 3D chemoattractant landscapes. *Nat. Commun.* **6**, 7985 (2015).
11. L. Alvarez, B. M. Friedrich, G. Gompper, U. B. Kaupp, The computational sperm cell. *Trends Cell Biol.* **24**, 198–207 (2014).
12. B. M. Friedrich, F. Jülicher, Steering chiral swimmers along noisy helical paths. *Phys. Rev. Lett.* **103**, 068102 (2009).
13. B. Ten Hagen, F. Kümmel, R. Wittkowski, D. Takagi, H. Löwen, C. Bechinger, Gravitaxis of asymmetric self-propelled colloidal particles. *Nat. Commun.* **5**, 4829 (2014).
14. G. Saggiorato, L. Alvarez, J. F. Jikeli, U. B. Kaupp, G. Gompper, J. Elgeti, Human sperm steer with second harmonics of the flagellar beat. *Nat. Commun.* **8**, 1415 (2017).
15. R. Nosrati, A. Driouchi, C. M. Yip, D. Sinton, Two-dimensional slither swimming of sperm within a micrometre of a surface. *Nat. Commun.* **6**, 8703 (2015).
16. P. Denissenko, V. Kantsler, D. J. Smith, J. Kirkman-Brown, Human spermatozoa migration in microchannels reveals boundary-following navigation. *Proc. Natl. Acad. Sci. U.S.A.* **109**, 8007–8010 (2012).
17. V. Kantsler, J. Dunkel, M. Blayney, R. E. Goldstein, Rheotaxis facilitates upstream navigation of mammalian sperm cells. *eLife* **3**, e02403 (2014).
18. S. S. Suarez, M. Wu, Microfluidic devices for the study of sperm migration. *MHR Basic Sci. Reprod. Med.* **23**, 227–234 (2016).
19. Z. Zhang, J. Liu, J. Meriano, C. Ru, S. Xie, J. Luo, Y. Sun, Human sperm rheotaxis: A passive physical process. *Sci. Rep.* **6**, 23553 (2016).
20. A. Bukatin, I. Kukhtevich, N. Stoop, J. Dunkel, V. Kantsler, Bimodal rheotactic behavior reflects flagellar beat asymmetry in human sperm cells. *Proc. Natl. Acad. Sci. U.S.A.* **112**, 15904–15909 (2015).
21. C.-k. Tung, F. Ardon, A. Roy, D. L. Koch, S. S. Suarez, M. Wu, Emergence of upstream swimming via a hydrodynamic transition. *Phys. Rev. Lett.* **114**, 108102 (2015).
22. J. Elgeti, R. G. Winkler, G. Gompper, Physics of microswimmers—Single particle motion and collective behavior: A review. *Reports Prog. Phys.* **78**, 56601 (2015).
23. C.-k. Tung, L. Hu, A. G. Fiore, F. Ardon, D. G. Hickman, R. O. Gilbert, S. S. Suarez, M. Wu, Microgrooves and fluid flows provide preferential passageways for sperm over pathogen *Tritrichomonas foetus*. *Proc. Natl. Acad. Sci. U.S.A.* **112**, 5431–5436 (2015).
24. M. Zaferani, S. H. Cheong, A. Abbaspourrad, Rheotaxis-based separation of sperm with progressive motility using a microfluidic corral system. *Proc. Natl. Acad. Sci. U.S.A.* **115**, 8272–8277 (2018).
25. S. S. Suarez, Sperm transport and motility in the mouse oviduct: Observations in situ. *Biol. Reprod.* **36**, 203–210 (1987).
26. R. P. Demott, S. S. Suarez, Hyperactivated sperm progress in the mouse oviduct. *Biol. Reprod.* **46**, 779–785 (1992).
27. A. P. Berke, L. Turner, H. C. Berg, E. Lauga, Hydrodynamic attraction of swimming microorganisms by surfaces. *Phys. Rev. Lett.* **101**, 038102 (2008).
28. T. D. Frank, *Nonlinear Fokker-Planck Equations: Fundamentals and Applications* (Springer Science & Business Media, 2005).
29. A. Guidobaldi, Y. Jeyaram, I. Berdakin, V. V. Moshchalkov, C. A. Condat, V. I. Marconi, L. Giojalas, A. V. Silhanek, Geometrical guidance and trapping transition of human sperm cells. *Phys. Rev. E* **89**, 032720 (2014).
30. R. Nosrati, P. J. Graham, Q. Liu, D. Sinton, Predominance of sperm motion in corners. *Sci. Rep.* **6**, 26669 (2016).
31. B. Saleh, *Introduction to Subsurface Imaging* (Cambridge University Press, 2011).
32. Y. Xia, G. M. Whitesides, Soft lithography. *Annu. Rev. Mater. Sci.* **28**, 153–184 (1998).
33. H. Bruus, *Theoretical Microfluidics* (Oxford University Press, 2008).
34. J. R. Dormand, P. J. Prince, A family of embedded Runge-Kutta formulae. *J. Comput. Appl. Math.* **6**, 19–26 (1980).
35. S. Kim, S. J. Karrila, *Microhydrodynamics: Principles And Selected Applications* (Courier Corporation, 2013).
36. J. Gray, G. J. Hancock, The propulsion of sea-urchin spermatozoa. *J. Exp. Biol.* **32**, 802–814 (1955).
37. B. Rodenborn, C.-H. Chen, H. L. Swinney, B. Liu, H. P. Zhang, Propulsion of microorganisms by a helical flagellum. *Proc. Natl. Acad. Sci. U.S.A.* **110**, E338–E347 (2013).
38. S. J. Lighthill, *Mathematical Biofluiddynamics* (SIAM, 1975).
39. D. Kleppner, R. Kolenkow, *An Introduction to Mechanics* (Cambridge University Press, 2013).
40. H. Risken, in *The Fokker-Planck Equation* (Springer, 1996), pp. 63–95.

Acknowledgments: We thank S. H. Cheong for providing the frozen bull semen samples and phase-contrast microscopy. We thank S. Suarez for reading the paper and for intellectual inputs. We also acknowledge D. Koch for the very helpful discussions about hydrodynamic interactions and lubrication approximation. We also thank M. Godec for intellectual inputs and for proofreading the paper, F. Javi for intellectual inputs and assistance with the illustrations, and P. Xie, D. Keating, and A. Parrella for providing the human sperm sample. **Funding:** This work was performed in part at the Cornell NanoScale Facility, a member of the National Nanotechnology Coordinated Infrastructure (NNCI), which is supported by the National Science Foundation (grant ECCS-1542081). **Author contributions:** M.Z. and A.A. designed research; M.Z. performed research; M.Z. analyzed data; M.Z., G.D.P., and A.A. wrote the paper; G.D.P. provided intellectual input about biological aspects of the research; and A.A. was the principal investigator of the group. **Competing interests:** The authors declare that they have no competing interests. **Data and materials availability:** All data needed to evaluate the conclusions in the paper are present in the paper and/or the Supplementary Materials. Additional data related to this paper may be requested from the authors.

Submitted 24 August 2018
Accepted 7 January 2019
Published 13 February 2019
10.1126/sciadv.aav2111

Citation: M. Zaferani, G. D. Palermo, A. Abbaspourrad, Strictures of a microchannel impose fierce competition to select for highly motile sperm. *Sci. Adv.* **5**, eaav2111 (2019).